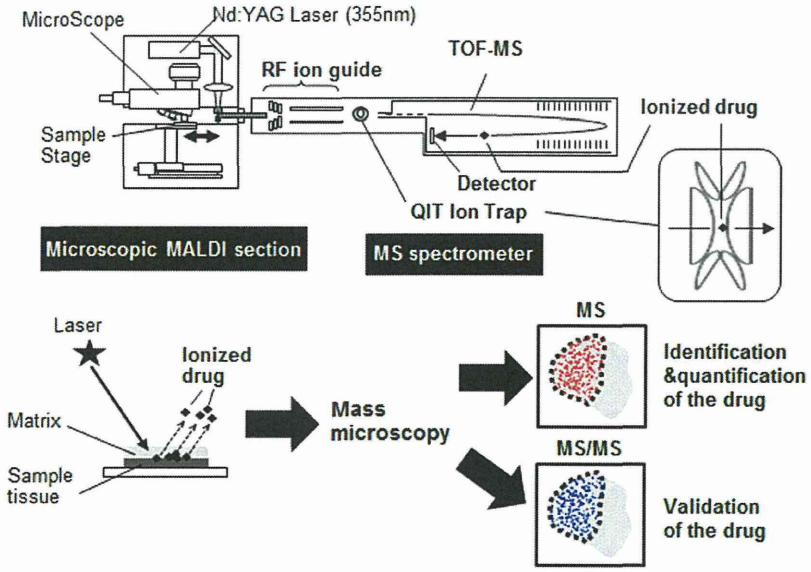

Figure 1 | Drug imaging system. A schematic illustration of the drug imaging system. The matrix-coated drug sample is ionised and then separated on the basis of its *m/z*. Images from MS or MS/MS analysis are recorded.

Results

The drug imaging system and its application in PTX analysis on the MALDI target. A schematic representation of our drug imaging system is shown in Fig. 1. Imaging data were acquired using a mass microscope. In the analysis, mass spectrometry (MS) and tandem mass spectrometry (MS/MS) were used for quantification and validation, respectively (Fig. 1).

Paclitaxel (PTX) is a mitotic inhibitor and an ACA that is used to treat various cancers. However, PTX is associated with peripheral neuropathy, a serious adverse affect[13]. NK105, a PTX-incorporating micelle, was developed to address this limitation of PTX[14–17]. On the basis of the enhanced permeability and retention (EPR) effect[17–20], NK105 can be selectively delivered to a tumour, resulting in an enhanced antitumour effect and the minimisation of adverse effects, including peripheral neuropathy. The high efficacy and low toxicity of NK105 have been demonstrated in both preclinical and clinical studies[14–17]. Although the administered drug content per tissue weight can be determined by conventional HPLC or LC-MS, the detailed drug distribution within the tumour and normal tissue has not been examined. Therefore, we used our drug imaging system to evaluate the difference in the distribution of NK105 and free PTX within tumour and normal peripheral neuronal tissue.

Antitumour activity and visualisation of PTX and NK105 distribution within the tumour with MS analysis. NK105 or PTX was administered at a PTX equivalent dose of 50 mg/kg/day to mice bearing BxPC3 pancreatic cancer xenografts on days 0, 4, and 8. NK105 showed significantly higher antitumour activity than the control (saline) and free PTX (Fig. 2a). To confirm the correlation of the distribution with the antitumour effect, the corresponding tumour sections were subjected to MALDI-IMS. A drug signal originating from PTX was detected in the tumours at 15 min and 1 h after the administration of PTX, but this signal decreased at 6 h and was below the limit of detection by 24 h (Fig. 2b). By contrast, the signal originating from the PTX released from NK105 (rPTX) following the accumulation of NK105 in the tumour was detected at 15 min as well as at 1, 24, 48, and 72 h after the administration of NK105. The signal intensity was greatest at 24 h (Fig. 2c). Tissue sections serial to those for MALDI-MS were also quantified by LC-MS (Fig. 2d, e), the results of which correlated with the drug imaging results (Fig. 2b–e). The data did not contradict previous data obtained by HPLC[14]. The results of the MALDI-MS analysis demonstrate that significant levels of PTX were present in the tumour clusters, including within the centre of the tumour tissue.

Validation of the PTX and NK105 distribution within tumour tissue by MS/MS analysis. Validation of the PTX content in each sample was performed in MS/MS mode. A structural diagram and the MS/MS fragmentation pattern (FP) of PTX are shown in Fig. 3a and b, respectively. According to the MS/MS-FP, *m/z* 607.19, which was selected as a PTX-specific fragment peak (Fig. 3c), was observed at a higher level in the tumour tissue sample at 1 h after PTX injection than at 1 h after NK105 injection (Fig. 3d, e).

Peripheral neurotoxicity and visualisation of the PTX and NK105 distribution by MS analysis. Next, a mechanical stress test that measured the degree of peripheral neurotoxicity demonstrated that the mice in the PTX treatment group exhibited a significantly stronger hypersensitive reaction to the mechanical stress test than those in the control and NK105 treatment groups (Fig. 4a). To confirm the correlation of the distribution with the abnormal neurological reaction, we also applied MALDI-IMS and examined the distribution of PTX in peripheral neural tissue at 30 min, 1 h, and 24 h after administration. The signals surrounding and inside the nerve were lower after NK105 injection than after PTX injection (Fig. 4b, c). LC-MS analysis of the neural samples revealed that the concentration of rPTX after NK105 injection was also lower than that after PTX injection (Fig. 4d).

Discussion

Conventional MALDI-IMS was expected to aid in the analysis of the global distribution of drugs within tissue. However, its application has been limited for a variety of reasons, including its limited resolution[7,8]. Recent progress in MALDI-IMS analysis, including the new features of our instrument, have achieved a MALDI-IMS resolution of 10 μm or less, which is advantageous for evaluating the drug distribution in specific cells or areas of interest within tissues[9–12]. The improved resolution also allows an IMS image to be overlaid on an optical image of the same sample. In fact, we were able to distinguish the nerve component from the surrounding tissue and evaluate the specific distribution of PTX in the region.

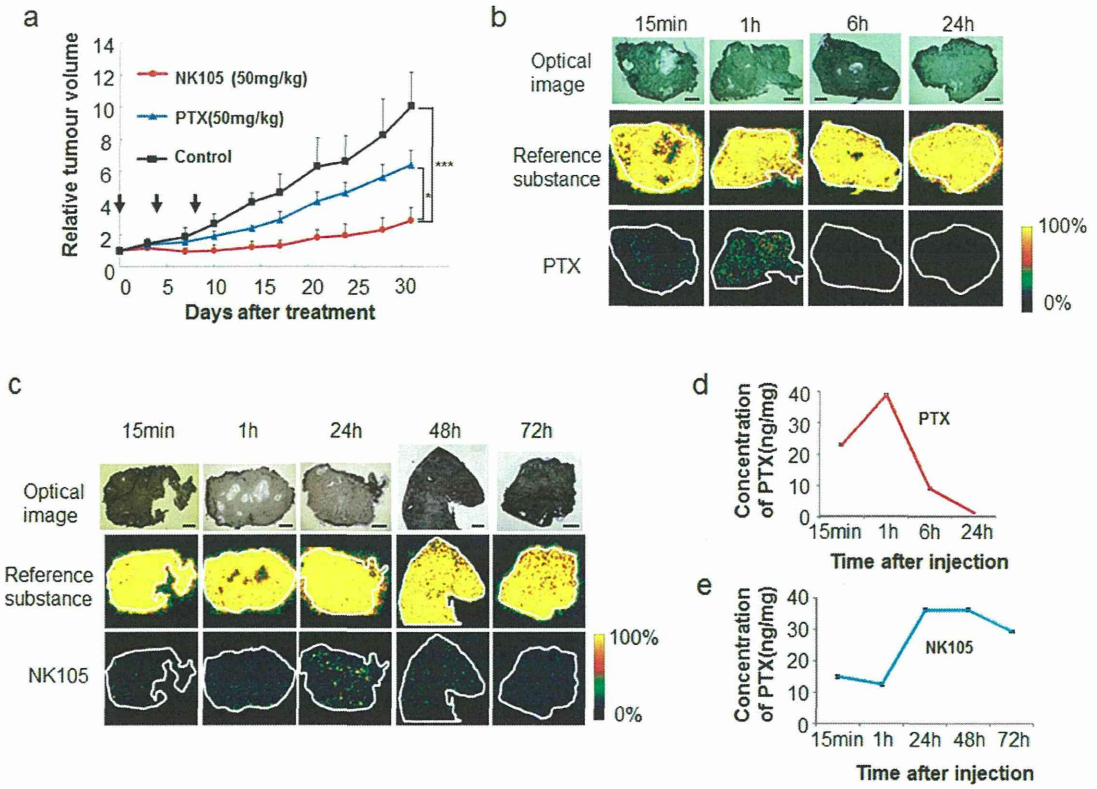

Figure 2 | Antitumour activity and visualisation of PTX and NK105 distribution with MS analysis. (a) Antitumour activity was examined in an animal model with BXPC3 xenografts. NK105, PTX, or saline (as a control) was administered at a PTX equivalent dose of 50 mg/kg on days 0, 4, and 8. *$P < 0.05$ (PTX vs. NK105), ***$P < 0.001$ (saline vs. NK105). Bar = SD. (b)(c) Imaging of PTX within the tumour was performed after PTX (b) or NK105 (c) administration at a dose of 100 mg/kg. The upper, middle, and lower columns display the optical images, reference substance (an arbitrary signal of m/z 824.6), and PTX (specific signal of m/z 892.3 $[M + K]^+$), respectively. Bar, 1 mm. (d)(e) LC-MS analysis of the PTX concentration in the tumours treated by PTX (d) or NK105 (e). Tissue sections serial to those shown in (b) and (c).

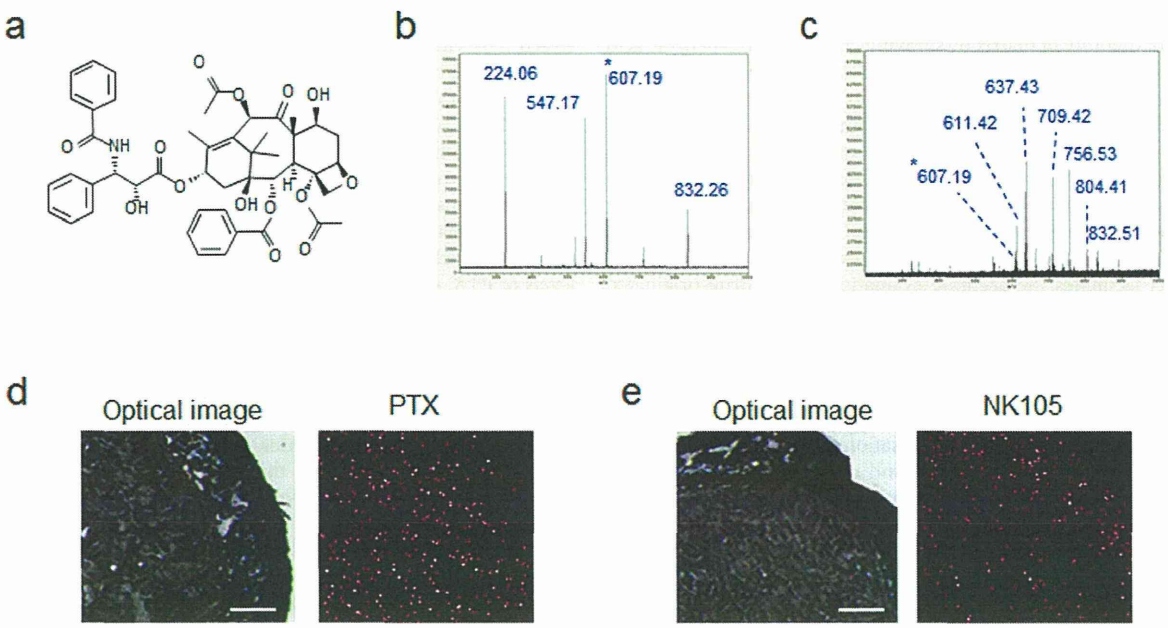

Figure 3 | Validation of the PTX and NK105 distribution within the tumour tissues by MS/MS analysis. (a) The structure of PTX is shown. (b) (c) The PTX-specific MS/MS fragments at m/z 224.06, 547.17, 607.19, and 832.26 are shown in (b). The fragment pattern from MS/MS analysis of the tumour tissue sample is shown in (c). (d) (e) Images obtained by optical microscopy (left) and by MS/MS analysis of PTX (m/z 607.19*) (right) in tumours treated with PTX (d) or NK105 (e) at 1 h after injection. Bar, 500 μm.

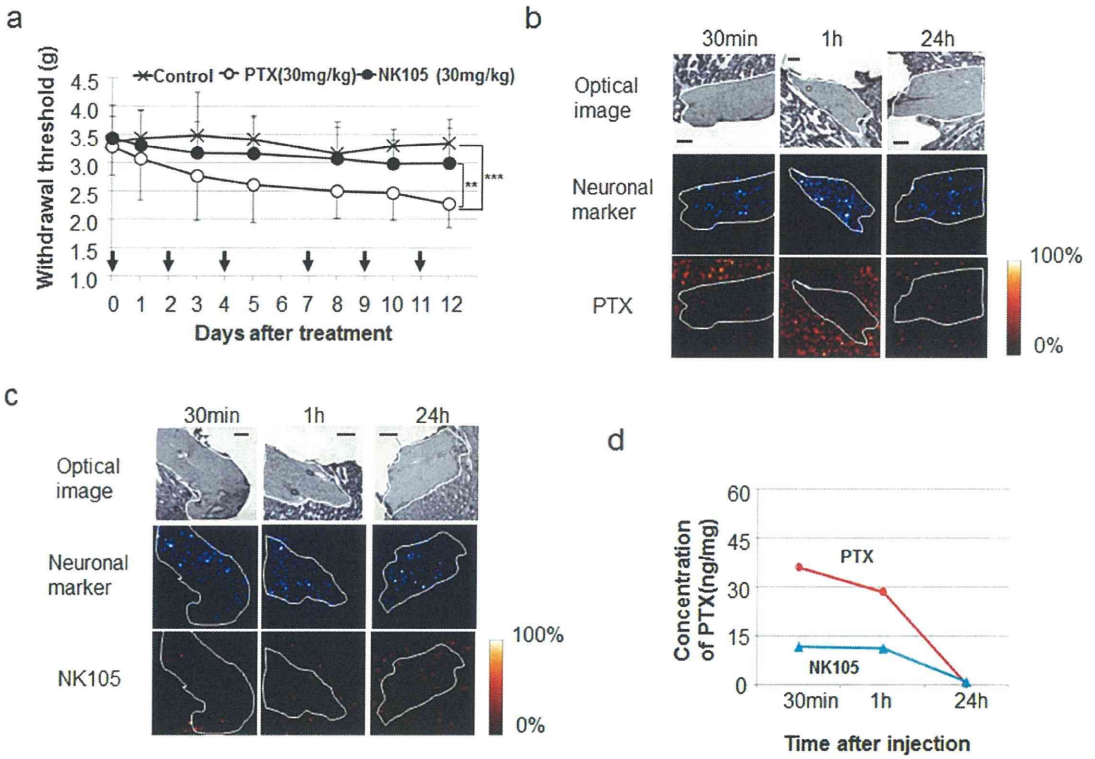

Figure 4 | Peripheral neurotoxicity and visualisation of PTX and NK105 distribution by MS analysis. (a) Mechanical sensory stress was assayed in an animal model of PTX-induced peripheral neuropathy. NK105, PTX, or saline was administered at 30 mg/kg on days 0, 2, 4, 7, 9, and 11. $^{**}P < 0.01$ (PTX vs. NK105), $^{***}P < 0.001$ (saline vs. PTX). Bar = SD. (b) (c) PTX within neuronal tissue was imaged after PTX (b) or NK105 (c) administration at a dose of 50 mg/kg. The upper, middle, and lower columns show the optical images, a neuronal marker (sphingomyelin-specific signal of 851.6 *m/z*), and PTX (specific signal of *m/z* 892.3 $[M + K]^+$), respectively. The neuronal area is delineated by a white line. Bar, 200 μm. (d) Analysis of the PTX concentration by LC-MS. Tissue sections serial to those shown in (b) and (c).

Tissue samples should be frozen without liquid solution to avoid the diffusion or loss of the drug from the tissue to the solution. For efficient ionisation in the present study, the sample was coated with a sufficient quantity of matrix by spraying. 2,5-Dihydroxybenzoic acid (DHB) was selected as the matrix to facilitate the efficient ionisation of the drug. We are now attempting to use several other matrix materials to enhance the sensitivity of our MALDI-IMS technique. Moreover, we used a combination of MS and MS/MS for the imaging analysis. In the MS analysis, accurate quantification of PTX was demonstrated in vivo. In the MS/MS analysis, the presence of PTX was validated by a fragment-specific signal at 607.19 *m/z*, which does not overlap with any other signals. The combination of MS and MS/MS thus facilitates the accurate evaluation of the drug-originated signal by distinguishing the drug signal from endogenous metabolites with a similar m/z.

In this report, MALDI-IMS demonstrated that NK105 successfully delivered a large amount of the PTX payload within the tumour tissue after NK105 injection compared with PTX injection alone. More importantly, the precise localisation and levels of PTX within the tumour tissue were visualised and quantified due to the high resolution of the MALDI-IMS technique. The obtained data did not contradict our MS data or previous data obtained by conventional pharmacological analysis using HPLC[14]. Thus, our data demonstrated that the antitumour activity of NK105 is superior to that of PTX alone. In addition, the peripheral neurotoxicity of NK105 was significantly lower than that of PTX, consistent with the MALDI-IMS data. In fact, in a phase 2 clinical trial of NK105 in patients with previously treated advanced stomach cancer, only one of the 56 patients (1.8%) who entered the trial experienced grade 3 peripheral neuropathy[16]. Phase 2 trials of other PTX formulations, including Abraxane and conventional PTX, have demonstrated that the incidence of grade 3 or 4 peripheral neuropathy is greater than 10%[21,22]. A phase 3 clinical trial of NK105 vs. PTX is now underway, which may elucidate the clinical significance of this micellar drug delivery system (DDS).

Although many studies have indicated that NK105 accumulates selectively in tumour tissue compared to PTX by HPLC or LC-MS analysis, whether NK105 could deliver PTX to cancer-cell clusters within the tumour tissue was unknown. Cancer tissue is heterogeneous and consists not only of cancer cells but also of abundant tumour stroma, the latter of which can act as a barrier against macromolecules, including NK105[23,24]. In the present study, significant levels of PTX, even in the core of the tumour tissue, were observed following NK105 administration, and the NK105 was retained for a long period of time.

Low molecular weight (LMW) ACAs, including molecular targeting agents, can easily extravasate from normal blood vessels and cause various adverse effects. DDS drugs such as NK105, which exhibit low short-term accumulation in normal tissues that lack the EPR effect, can minimise this drug toxicity. Our data clearly demonstrate that the distribution of rPTX from NK105 in the peripheral nerve and surrounding tissues was quite low compared with PTX alone. These observations support the low incidence of peripheral neuropathy when PTX is administered as NK105.

This is the first report describing the precise distribution of a DDS drug by MSI, a new technique developed by our lab and others. Notably, we successfully visualise and quantified the distribution of a non-radiolabeled and non-chemically modified drug in various frozen tissue slices microscopically. In addition to PTX, we have successfully visualised other anticancer agents, including SN-38,

epirubicin, and monomethyl auristatin E (MMAE) (data not shown). This success indicates that the MALDI-IMS technique can be applied to clinical biopsy specimens or surgically resected tissues after neo-adjuvant chemotherapy. In addition, the data obtained by MALDI-IMS can be utilised to facilitate drug design.

Methods

Cells and reagents. The human pancreatic cancer cell line BxPC3 was purchased from the American Type Culture Collection and maintained in DMEM (Sigma, St. Louis, MO) supplemented with 10% foetal bovine serum (Tissue Culture Biologicals, CA), penicillin, streptomycin, and amphotericin B (Sigma) at 5% CO_2 and 37°C. NK105, a PTX-incorporating 'core-shell-type' polymeric micellar nanoparticle, was supplied by Nippon Kayaku Co. Ltd. (Tokyo, Japan). The weight-average diameter of the nanoparticles was approximately 85 nm, ranging from 20 to 430 nm. PTX was purchased from Tokyo Chemical Industry Co. (Tokyo, Japan).

Drug imaging by mass microscopy. IMS analysis was performed using an atmospheric pressure (AP) MALDI-IT-TOF mass spectrometer (prototype Mass Microscope; Shimadzu)[25].

To prepare tissue samples, the tumour and sciatic nerve with surrounding tissue were surgically removed from a xenograft model at 15 min, 30 min, 1 h, or 24 h after drug administration (50 or 100 mg/kg). Samples wrapped in gauze were frozen in dry ice powder. The samples were then sectioned at a thickness of 10 μm and transferred to an indium tin oxide-coated glass slide (Sigma). The tissue section was dried (with no washing step) before matrix coating.

For the application of the matrix onto the tissue slide, 30 and 50 mg/ml of DHB in 50% methanol and 0.1% trifluoroacetic acid were used. The 30 mg/ml DHB solution (0.4 ml) was sprayed twice, and then the 50 mg/ml (0.4 ml) solution was sprayed once with a 0.2-mm nozzle calibre airbrush (Procon Boy FWA Platinum; Mr. Hobby, Tokyo, Japan); each spraying step was completed over 5 min. During spraying, the distance between the nozzle and the tissue surface was maintained at 15 cm to keep the surface dry.

IMS analyses were performed in positive-ion mode within a mass range of *m/z* 720–920 for PTX, with a spatial resolution of 30 μm. The laser was irradiated at 40 shots/spectrum at a frequency of 400 Hz, and the power was set to 60–65% using the Mass Microscope operation software. PTX distribution mapping was performed in BioMap (Novartis, Basel, Switzerland) using the *m/z* 892.3 ($[M + K]^+$) signal because the ($[M + K]^+$ signal showed more sensitive mass spectra than did the $[M + H]^+$ and $[M + Na]^+$ signals. The uniformly distributed *m/z* 824.6 ion (corresponding to cerebrosides (42 : 6) + Na) in tumour sections and *m/z* 851.6 ion (sphingomyelin (d18 : 1/24 : 1) + K) in neuronal tissue were used as internal controls to correct the PTX signal intensity.

MS/MS analysis of PTX (*m/z* 892.3) was performed with the CID function of the quadruple ion trap cell on the Mass Microscope. The *m/z* 607.19 fragment ion was generated on the tissue. This ion was also observed for the authentic PTX as the derivative and was used for MS/MS imaging of the drug. The instrument conditions for MS/MS imaging were identical to those used for the MS mapping described above, but the spatial resolution was 15 μm, and the laser power was 50%.

Animal model. *Antitumour activity.* Female BALB/c nude mice (5 weeks old) and DBA/2N mice (8 weeks old) were purchased from SLC Japan (Shizuoka, Japan). The nude mice were inoculated subcutaneously in the flank with 1×10^6 BxPC3 cells. The length (L) and width (W) of the tumour masses were measured every 3 to 4 days, and the tumour volume was calculated using the following formula: $(L \times W^2)/2$. When the mean tumour volume reached approximately 300 mm^3, the mice were randomly assigned to groups of five. Drugs (50 mg/kg) were administered on days 0, 4, and 8 by injection into the mouse tail vein.

Peripheral neuropathy. To investigate the neurotoxicity induced by PTX and NK105, we designed the following experimental scheme: The development of nocifensive responses to mechanical stimuli was assessed in the mice (ref). Six-week-old female DBA/2N mice were randomly assigned to one of three groups, and their baseline nocifensive responses were measured. We confirmed that the mean latency was statically identical between the groups. The mice were then administered a dose of 30 mg/kg PTX or 30 mg/kg NK105 on days 0, 2, and 4 every week for 2 weeks, for a total of 6 injections (n = 10). Control mice were injected with 5% dextrose solution on the same schedule. After a total of 6 administrations, the mice were tested for transitional changes in their nocifensive responses. Mechanical allodynia was assessed by measuring the latency of paw withdrawal in response to noxious mechanical stimuli using a Dynamic Plantar Aesthesiometer (Ugo Basile, Varese, Italy). The mice were placed on a wire mesh floor in individual Plexiglas cages and were allowed to acclimate for approximately 1 h, during which exploratory and grooming activity was completed. The mechanical stimulus was applied to the plantar aspect of the hind paw using a 2-mm-diameter metal filament. The force was automatically increased at a fixed rate (0–5 g, 0.25 g/sec) until the mouse withdrew its paw. The analysis of paw withdrawal responses was repeated 4 times at 10-sec intervals. The paw withdrawal threshold (g) was determined from the average of the four measurements. None of the mice in this assay were inoculated with tumour cells.

All animal procedures and experiments were approved by Committee for Animal Experimentation of the National Cancer Centre, Tokyo Japan.

These guidelines meet the ethical standards required by law and comply with the guidelines for the use of experimental animals in Japan.

Statistical analysis was performed using analysis of variance (ANOVA) with Tukey's multiple comparison tests.

LC-MS. For LC-MS, several sections immediately adjacent to the sections for IMS imaging were serially collected into a vial, and the drug was extracted into acetonitrile by vortexing. The samples were analysed with a Liquid Chromatograph Mass Spectrometer LCMS-8040 (Shimadzu Corp.). A Kinetex 2.6 μm C18 100A (100 × 2.1 mm) analytical column was used. The injection volume was 1 μl, and the flow rate was 0.5 ml/min. (A) Acetonitrile and (B) 0.1% (w/v) formic acid solution were used as the mobile phases. The mobile phase was introduced into the spectrometer via electrospray ionisation in positive ion mode under multiple reaction monitoring (MRM) conditions. In terms of the gradient, acetonitrile was conducted at 50% (B) for the first 1.5 min, increased to 100% for 0.25 min, and subsequently decreased back to 50% for 1.25 min. The PTX quantification was performed with the precursor *m/z* 854.45 ion, and the standard curve generated using the product *m/z* 104.95 ion was used. The data were collected in triplicate experiments.

1. Chin, L. & Gray, J. W. Translating insights from the cancer genome into clinical practice. *Nature* **452**, 553–563 (2008).
2. Van Dort, M. E., Rehemtulla, A. & Ross, B. D. PET and SPECT Imaging of Tumor Biology: New Approaches towards Oncology Drug Discovery and Development. Curr. Comput. *Aided Drug Des.* **4**, 46–53 (2008).
3. Garrett, M. D. & Workman, P. Discovering novel chemotherapeutic drugs for the third millennium. *Eur. J. Cancer* **35**, 2010–2030 (1999).
4. Abramson, R. G. *et al.* Complications of targeted drug therapies for solid malignancies: manifestations and mechanisms. *AJR Am J Roentgenol.* **200**, 475–483 (2013).
5. Horak, C. E. *et al.* Biomarker analysis of neoadjuvant doxorubicin/cyclophosphamide followed by ixabepilone or Paclitaxel in early-stage breast cancer. *Clin. Cancer Res.* **19**, 1587–1595 (2013).
6. Waddell, T. & Cunningham, D. Impact of targeted neoadjuvant therapies in the treatment of solid organ tumours. *Br. J. Surg.* **100**, 5–14 (2013).
7. Cornett, D. S., Reyzer, M. L., Chaurand, P. & Caprioli, R. M. MALDI imaging mass spectrometry: molecular snapshots of biochemical systems. *Nat. Methods* **4**, 828–833 (2007).
8. Schwamborn, K. & Caprioli, R. M. Molecular imaging by mass spectrometry--looking beyond classical histology. *Nat. Rev. Cancer* **10**, 639–646 (2010).
9. Castellino, S., Groseclose, M. R. & Wagner, D. MALDI imaging mass spectrometry: bridging biology and chemistry in drug development. *Bioanalysis* **3**, 2427–2441 (2011).
10. Saito, Y. *et al.* Development of imaging mass spectrometry. *Biol. Pharm. Bull.* **35**, 1417–1424 (2012).
11. Lorenz, M., Ovchinnikova, O. S., Kertesz, V. & Van Berkel, G. J. Laser microdissection and atmospheric pressure chemical ionisation mass spectrometry coupled for multimodal imaging. *Rapid Commun Mass Spectrom.* **27**, 1429–1436 (2013).
12. Römpp, A. & Spengler, B. Mass spectrometry imaging with high resolution in mass and space. *Histochem Cell Biol.* **139**, 759–783 (2013).
13. Rowinsky, E. K. *et al.* Phase I and pharmacologic study of paclitaxel and cisplatin with granulocyte colony-stimulating factor: neuromuscular toxicity is dose-limiting. *J. Clin. Oncol.* **11**, 2010–2020 (1993).
14. Hamaguchi, T. *et al.* NK105, a paclitaxel-incorporating micellar nanoparticle formulation, can extend in vivo antitumour activity and reduce the neurotoxicity of paclitaxel. *Br. J. Cancer* **92**, 1240–1246 (2005).
15. Hamaguchi, T. *et al.* A phase I and pharmacokinetic study of NK105, a paclitaxel-incorporating micellar nanoparticle formulation. *Br J Cancer* **97**, 170–176 (2007).
16. Kato, K. *et al.* Phase II study of NK105, a paclitaxel-incorporating micellar nanoparticle, for previously treated advanced or recurrent gastric cancer. *Invest. New Drugs* **30**, 1621–1627 (2012).
17. Matsumura, Y. & Kataoka, K. Preclinical and clinical studies of anticancer agent-incorporating polymer micelles. *Cancer Sci.* **100**, 572–579 (2009).
18. Matsumura, Y. & Maeda, H. A new concept for macromolecular therapeutics in cancer chemotherapy: mechanism of tumoritropic accumulation of proteins and the antitumor agent smancs. *Cancer Res.* **46**, 6387–6392 (1986).
19. Duncan, R. Polymer conjugates as anticancer nanomedicines. *Nat. Rev. Cancer* **6**, 688–701 (2006).
20. Peer, D. *et al.* Nanocarriers as an emerging platform for cancer therapy. *Nat. Nanotechnol.* **2**, 751–760 (2007).
21. Ibrahim, N. K. *et al.* Multicenter phase II trial of ABI-007, an albumin-bound paclitaxel, in women with metastatic breast cancer. *J Clin Oncol.* **23**, 6019–26 (2005).
22. Johnson, D. H., Chang, A. Y. & Ettinger, D. S. Taxol (paclitaxel) in the treatment of lung cancer: the Eastern Cooperative Oncology Group experience. *Ann Oncol.* **Suppl 6**, S45–50 (1994).
23. Matsumura, Y. Cancer stromal targeting (CAST) therapy. *Adv Drug Deliv Rev.* **64**, 710–719 (2012).
24. Dimou, A., Syrigos, K. N. & Saif, M. W. Overcoming the stromal barrier: technologies to optimize drug delivery in pancreatic cancer. *Ther Adv Med Oncol.* **5**, 271–279 (2012).

25. Harada, T. *et al.* Visualization of volatile substances in different organelles with an atmospheric-pressure mass microscope. *Anal Chem.* **81**, 9153–9157 (2009).

Acknowledgments

This work was supported by the Funding Program for World-Leading Innovative R&D on Science and Technology (FIRST Program) (YM), Third Term Comprehensive Control Research for Cancer from the Ministry of Health, Labour and Welfare of Japan (YM), a Grant-in-Aid for Scientific Research on Priority Areas from the Ministry of Education, Culture, Sports, Science and Technology, the National Cancer Center Research and Development Fund (YM and MY), the Kobayashi Foundation Research Grant for Cancer Research (MY), and a Grant-in-Aid for Scientific Research from the Japan Society for the Promotion of Science (MY). We thank Mrs K. Shiina for her secretarial support.

Author contributions

Y.M. developed the method. M.Y., M.F., K.O., Y.K., Y.Y. and M.T. performed the experiments and analysed the data. Y.M. and M.Y. wrote the manuscript.

Additional information

Competing financial interests: The authors declare no competing financial interests.

How to cite this article: Yasunaga, M. *et al.* The significance of microscopic mass spectrometry with high resolution in the visualisation of drug distribution. *Sci. Rep.* 3, 3050; DOI:10.1038/srep03050 (2013).

Microvascular Reviews and Communications

Vol.6 No.1

Tumor stromal barrier and cancer stromal targeting therapy

Masahiro Yasunaga[1)], Shino Manabe[2)] and Yasuhiro Matsumura[1),*]

1) Division of Therapeutic Development, Research Center for Innovative Oncology, National Cancer Center Hospital East

2) Synthetic Cellular Chemistry Laboratory, RIKEN

Abstract

Antibody drug conjugates (ADCs) are effective for tumors with no or little stroma, such as malignant lymphoma or breast cancer. However, in refractory cancers (pancreatic cancer or scirrhous gastric cancer) forming hypovascular and stroma-rich tumors, the penetration of monoclonal antibodies (mAbs) into the cells is impeded (stromal barrier), which leads to failure of conventional cell-targeting ADCs. To overcome this, we developed cancer stromal targeting (CAST) therapy using anti-collagen IV or anti-fibrin mAbs. These stroma-targeting ADCs selectively extravasated from leaky tumor vessels and bound to collagen IV or fibrin on the tumor stroma, from which effective sustained release of the payload drug occurred. The released drug subsequently diffused through the tumor tissue, causing marked arrest of tumor growth associated with damage to tumor vessels and death of cancer cells. In terms of the pathological findings after treatment, empty sleeves collagen IV-positive and CD31-negative remnant ring structures) were observed in the destroyed vessels. This review highlights the tumor stromal barrier and the development of CAST therapy. Insights into the pharmacokinetics and efficacy of antibodies or ADCs may also be informative to understand the pathophysiological role of the tumor microcirculation involved in the stromal barrier. [MVRC 6(1): 2-8, 2013]

Key words: cancer, stromal barrier, antibody, ADC, CAST

Received 2013/5/20, Accepted 2013/9/2

*To whom correspondence should be addressed: Dr. Yasuhiro Matsumura, Division of Therapeutic Development, Research Center for Innovative Oncology, National Cancer Center Hospital East, 6-5-1 Kashiwanoha, Kashiwa, Chiba 277-8577, Japan
E-mail: yhmatsum@east.ncc.go.jp

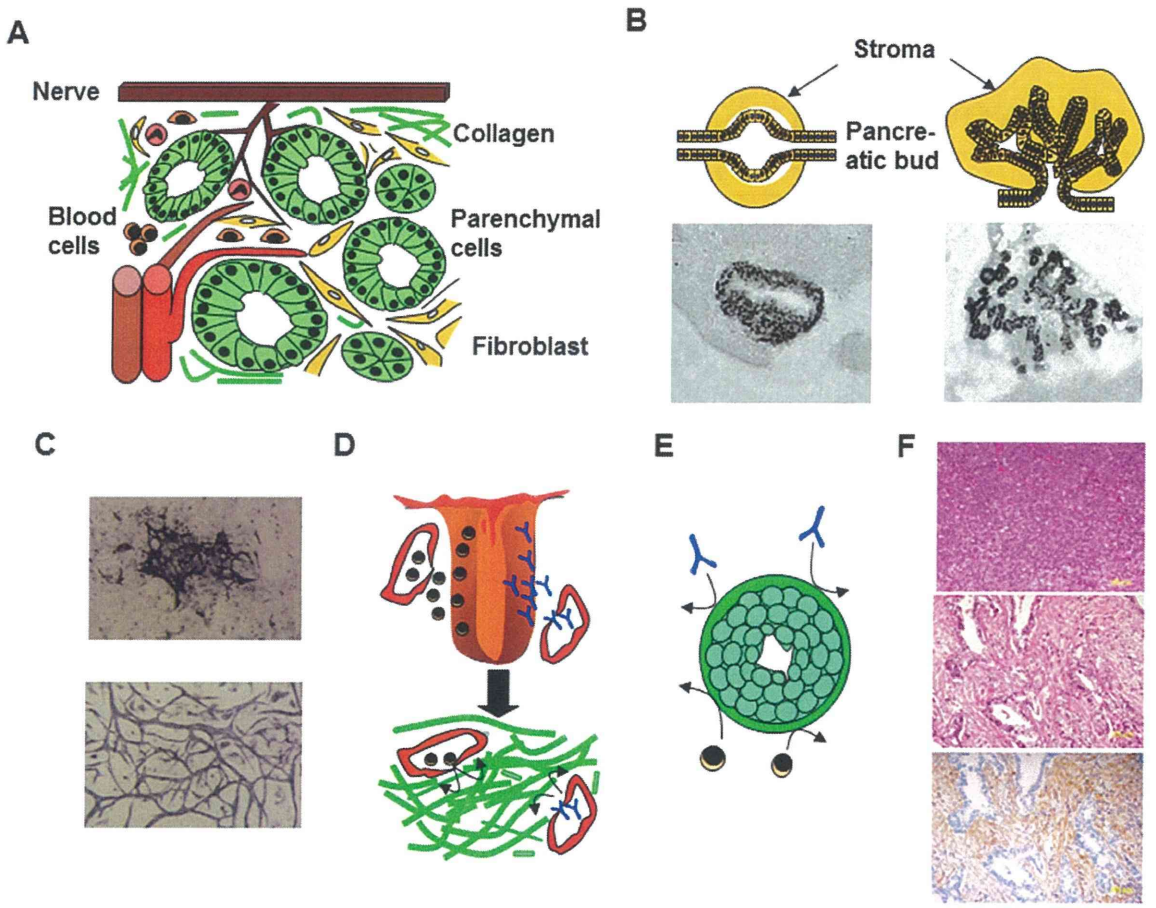

Fig. 1. Physiological and pathophysiological roles of stroma. (A) Parenchymal cells and stroma. (B) Pancreas organogenesis induced by stroma. (C) VEGF and collagen IV promote insufficient vasculogenesis (upper panel). Well-organized vascular tube formation occurred in the presence of stoma cells (lower panel). (D) Stroma suppresses overreaction of the inflammation. (E) Stroma defends the reproductive system against autoimmune attack. (F). Hematoxylin-eosin staining of malignant lymphoma (ML) (upper panel) and pancreatic cancer (PC) (middle panel). Immunostaining of stromal collagen IV (brown) in PC. Cancer cells were stained by eosin (blue) (lower panel).

Introduction

Although many monoclonal antibodies (mAbs) have already been approved for the treatment of cancer, they are usually used in combination with anticancer agents (ACAs) because of their limited anti-tumor activity when used alone[1]. Antibody-drug conjugates (ADCs), the next generation of therapeutic antibodies, are a promising strategy to enhance the cytotoxic effect[2–4]. Conventional ADCs depend on enzymatic cleavage following internalization into the cytoplasm or lysosome. Most human solid tumors, however, possess abundant stroma, which hinders the distribution of ADCs (stromal barrier). Moreover, the process of cell uptake is disturbed by the stromal barrier. Therefore, this barrier limits the effectiveness of ADCs, regardless of the internalization ability. The heterogeneity of tumor cells also prevents the development of ADC therapy based on a cell-specific antigen[5–8].

To overcome these issues, we created a unique type of ADC, namely, cancer stromal targeting (CAST) therapy, in which stroma-targeting mAbs (anti-collagen IV or anti-fibrin mAbs) were conjugated to cytotoxic ACAs[6–8]. Our ADC bound to collagen IV or fibrin in the stroma, from which sustained release of ACAs and their distribution throughout the tumor occurred; this had a strong anti-tumor effect against stroma-rich tumors compared with that of conventional ADCs[5–8].

In this article, we initially outline the tumor stromal barrier and conventional ADCs, followed by an introduction and discussion of CAST therapy.

Physiological and pathophysiological roles of stroma

Organ or tissue consists of not only parenchymal cells but also stroma. Stroma has various components such as fibroblasts, blood vessels, and nerve or extracellular matrix proteins, for example, collagen, fibrin and fibronectin (Fig. 1A). As a result, stroma exhibits various biological activities[9–12]. In embryogenesis, stroma can induce organogenesis of the pancreas, liver or lung (Fig. 1B). Regarding tissue remodeling, vasculogenesis by endothelial progenitors is promoted by collagen IV and VEGF, but the tube formation is insufficient, whereas well-organized vascular tube formation occurs in the presence of stroma cells (Fig. 1C). Upon inflammation, stroma blocks the overreaction of immune cells and terminates inflammatory process (Fig. 1D). Stroma also acts in host defense within the reproductive system (Fig. 1E).

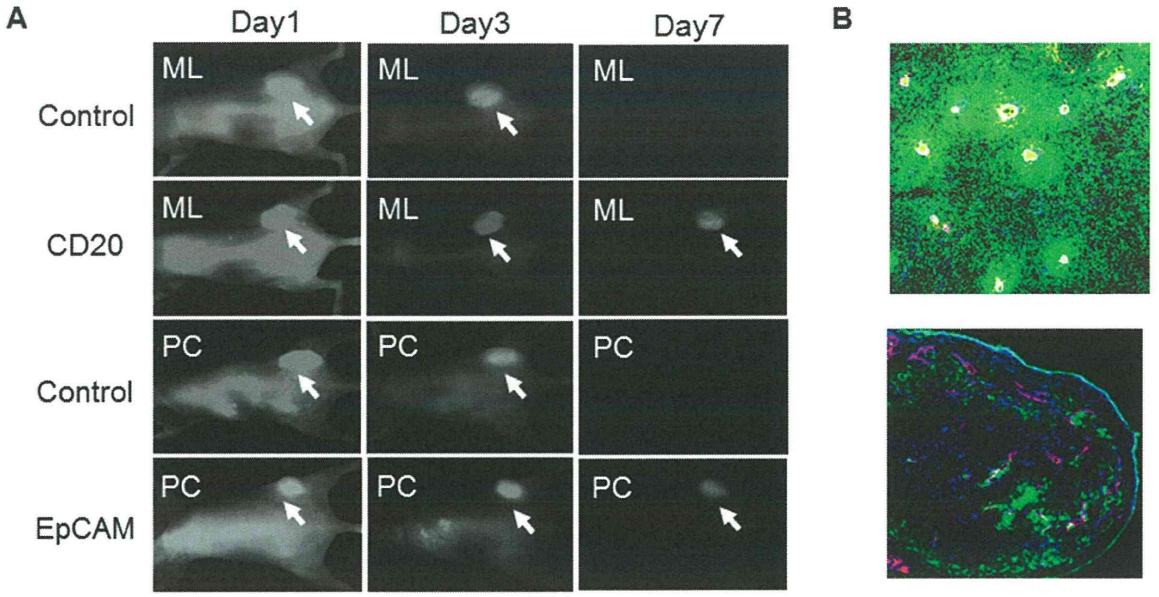

Fig. 2. Antibody delivery in malignant lymphoma and pancreatic cancer. (A) In vivo imaging of fluorescent mAbs. Anti-CD20 and anti-EpCAM mAbs were injected into malignant lymphoma (ML) and pancreatic cancer (PC) models, respectively. Non-specific mAb was used as a control. (B) Distribution of anti-CD20 mAb (green) and anti-EpCAM mAb (green) within ML tumor and PC tumor, respectively. Blood vessels (whitish-yellow in upper panel, magenta in lower panel) are shown.

In malignant tissues, stroma promotes the growth, survival, invasion or metastasis of tumor cells. It is thus increasingly important to understand the role of the stroma in tumorigenesis[13–17]. There are two distinct types of tumor tissue: those with little stroma, for example, malignant lymphoma (ML), and those with dense stroma, for example, pancreatic cancer (PC) (Fig. 1F), and the latter is strongly associated with the treatment-resistant phenotype.

Antibody drug conjugate and stromal barrier

Recently, several ADCs have been approved for oncological treatment[1–4]. These antibody therapies are effective for ML or breast cancer (BC), but not for refractory cancers such as PC or scirrhous gastric cancer (SGC). Although many researchers have investigated the molecular mechanism behind enhanced anti-apoptotic effect, the abundance of drug-efflux transporters or the existence of natural chemo-resistant cancer stem cells, in order to solve this question, the issue of the tumor stromal barrier has been almost entirely overlooked. We speculated that dense stroma prevents antibody distribution within tumor tissue, which would be one of the reasons for therapeutic resistance. Therefore, in a previous study, we evaluated antibody using an in vivo imaging system. We used two types of tumor model: ML and PC. Anti-CD20 mAb and anti-EpCAM mAb were also used as specific mAbs against ML and PC, respectively. In whole body imaging, both non-specific mAbs and specific mAbs accumulated in the tumor by an enhanced permeability and retention (EPR) effect[18] as passive targeting on Day 3 after injection (Fig. 2A). High-molecular-weight agents including mAbs were shown to extravasate from leaky tumor vessels but not normal tissues[18]. Moreover, they remained at the site for a long time because of the lack of effective lymphatic drainage, which impeded the efficient clearance of mAbs accumulated in solid tumor tissues[18]. On Day 7, although non-specific mAbs disappeared from the tumor, specific mAbs still accumulated there by utilizing their specific antigen-binding ability (Fig. 2A). We considered mAbs to be one of the ideal drug delivery system (DDS) carriers because IgG ranging in size from 10 to 20 nm can utilize the EPR effect[18]. Moreover, specific mAbs were able to stay longer by the EPR effect plus active targeting.

We then examined the mAb distribution within tumor tissue. Extravasated anti-CD20 mAbs were distributed throughout the whole tumor in ML, whereas the distribution of anti-EpCAM mAbs was restricted to the tumor margin adjacent to vessels in PC. A very small amount of mAb reached the central area within the tumor (Fig. 2B). This phenomenon can be explained by the stromal barrier. Although some authors reported that mAbs extravasted from leaky tumor vessels were able to reach the tumor cells sufficiently, they used hypervascular and stroma-less tumor models[19, 20]. We therefore considered these models were close to the ML rather than PC. On the other hand, genetic engineered mouse (GEM) models have come to be used for the studying human cancer[21]. The pancreatic tumors observed in the model displayed pathophysiological features similar to human pancreatic cancers. By using this model, it was shown that the dense stromal was able to prevent drug delivery into the tumor cells[23, 24]. We speculate that stromal barrier involves three factors: 1) mechanical interference by stromal cells and extracellular proteins, 2) pharmacological disturbance depending on low convection and diffusion, and 3) a long distance from vessels to tumor cells. We need to further investigate the mechanism of the stromal barrier to elucidate this hypothesis.

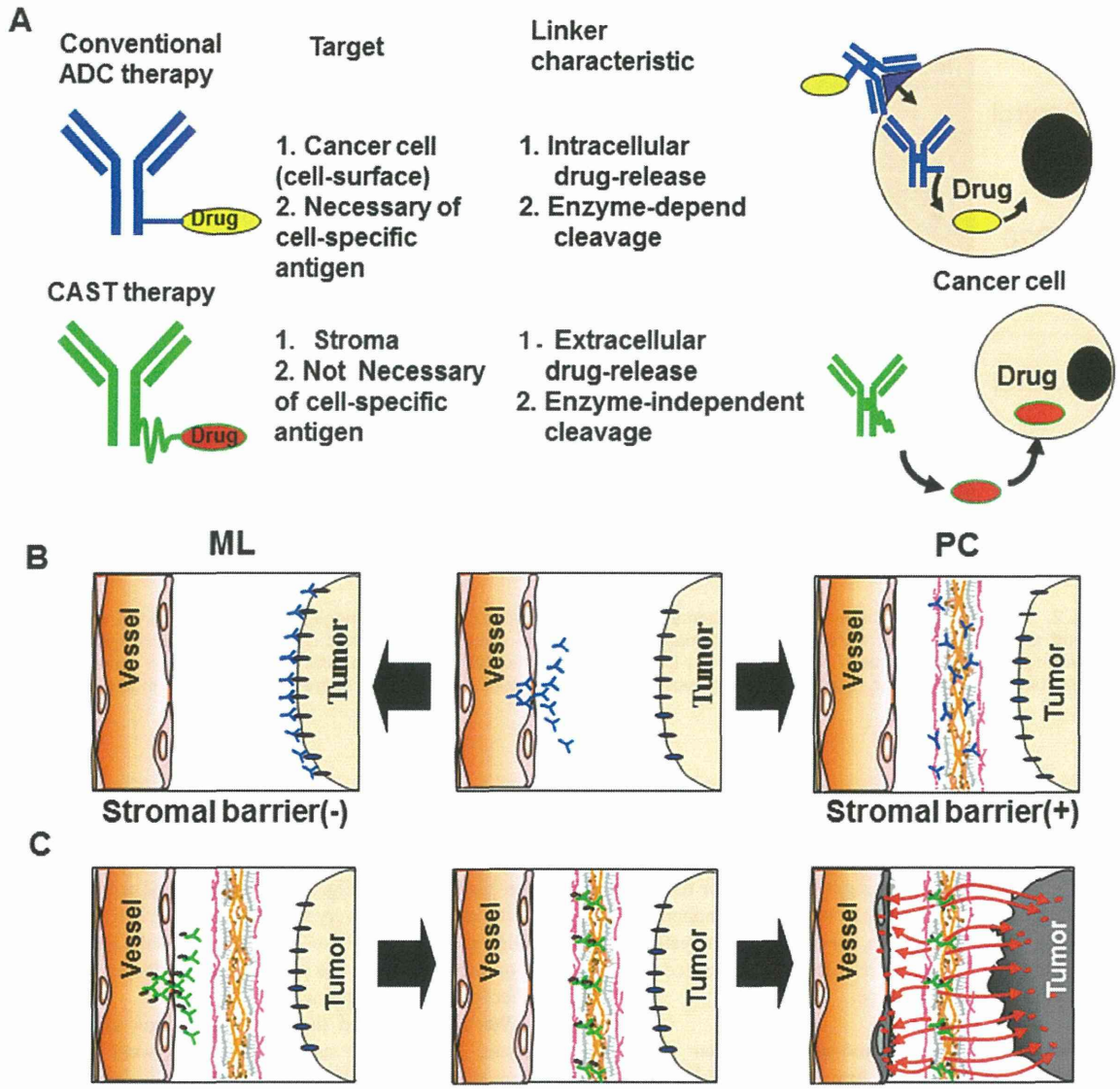

Fig. 3. Conventional ADC and CAST therapy. (A) Comparison between conventional ADC and CAST therapy. (B) Conventional ADC can be distributed and reach the tumor cell in the absence of a stromal barrier, but not in the presence of one. (C) CAST therapy ADC can accumulate on stroma, from which sustained release of the drug can occur and attack both tumor cells and tumor vasculature because a small molecule drug is not influenced by the stromal barrier.

Conventional ADCs

In the 1980s, the development of anti-tumor-cell-specific mAbs carrying a cytotoxic drug, known as missile therapy and expected to be a magic bullet for cancer treatment, was actively pursued. However, the induction of human anti-mouse antibody (HAMA) response was a major impediment to the success of antibody-related therapies. In addition, most of the linkers connecting the cytotoxic drug to an mAb were unstable and easily degraded in the body. Fortunately, recent progress in antibody engineering and linker technology has overcome these problems[1–4]. Chimeric or humanized mAb reduces the rate of HAMA reactions. In addition, linkers that are stable enough in the body to last until the ADC reaches the tumor cells, and also sufficiently cleavable to allow effective drug release within cells, have been successfully developed[2–3] (Fig. 3A and B). Recently, the clinical benefit of newly developed anti-HER2 mAb-DM1 has been demonstrated in the treatment of BC[4]. However, there is less stroma in BC than in refractory solid tumors such as PC or SGC. Moreover, most BCs are hypervascular tumors, in which the stromal barrier may be weakened. Furthermore, the treatment is limited to HER2-overexpressing tumors. Most human refractory solid tumors, however, possess hypovascularity and dense stroma that hinders the distribution of ADCs (Fig. 3B). ADCs can release drug by enzymatic cleavage after internalization into a cell and delivery to the lysosome. However, the stromal barrier in solid tumor prevents ADCs from reaching the cells. Unlike the limited cases of HER2-overexpressing BC, in most cases, heterogeneity of the tumor cells prevents the development of ADC therapy

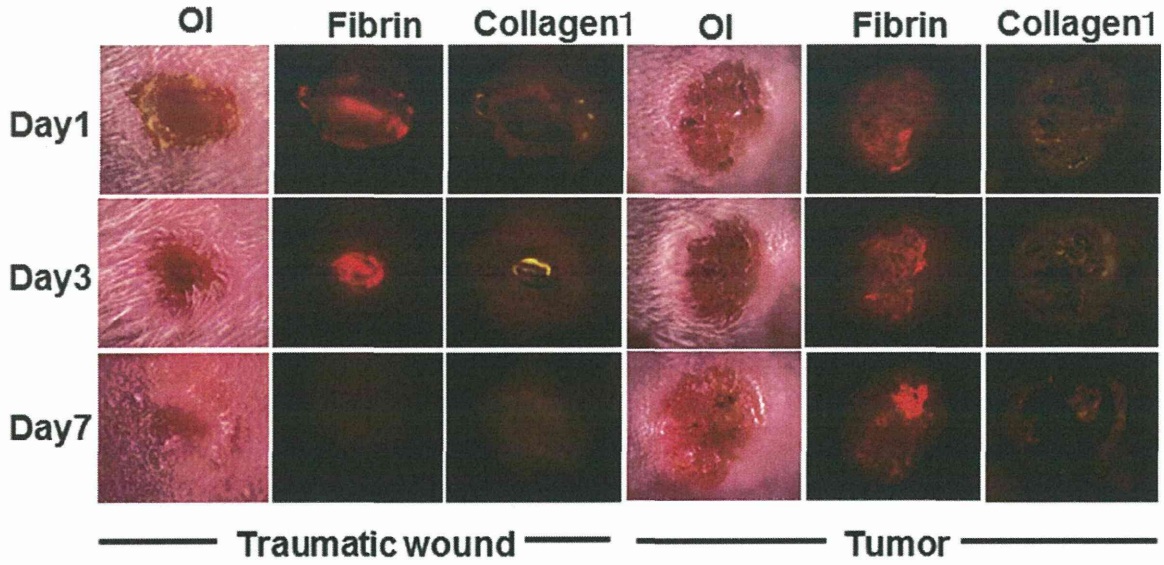

Fig. 4. Tumor specificity of anti-fibrin mAb. Biodistribution of Alexa 647-labeled anti-fibrin mAb (Red) and Alexa 555-labeled anti-collagen-1 mAb in mouse bearing a traumatic wound (left columns) and tumor (right columns) on days 1, 3 and 7 after the injection. OI: optical image.

based on a cell-specific antigen. It seems that conventional cell-targeting ADC therapy is effective for hematological malignancy (ML) or hypervascular solid tumors having little stroma (BC), but not for high-stromal hypovascular solid tumors (PC).

CAST therapy

To overcome the limitations of conventional ADCs, we created CAST therapy, which utilizes abundant stroma as a scaffold for drug delivery (Fig. 3A and C). It was composed of ACAs conjugated to stroma (collagen IV or fibrin)-targeting mAb via an ester-bond linker[6–8]. Our stroma-targeting ADCs were shown to reach tumor passively by the EPR effect[18]. Moreover, they bound to the tumor stroma, from which effective sustained release of ACAs occurred. The released ACAs could be distributed throughout the tumor because the ester bond could gradually be cut by hydrolysis (non-enzymatically) outside of the cells. Polyethylene glycol (PEG) adjacent to the ester bond protected the degradation of the bond in the blood before the tumor was reached. ACAs released from the ADCs were shown to damage both tumor cells and tumor vessels, which resulted in the arrest of tumor growth[6–8]. We focused on two stromal components, fibrin and collagen, the levels of which are generally high in tumors. In non-malignant diseases such as cerebrovascular disease, cardiac infarction, traumatic wound and rheumatoid arthritis, fibrin formation occurs at onset or during the active phase. At 7 days after onset, fibrin disappears and is replaced by collagen. A contracted collagenous scar is then formed as the final step of healing. On the other hand, in malignant tumor, bleeding, fibrin formation and collagen replacement as a malignant cycle of blood coagulation are reproduced as long as tumor cells exist and invade the adjacent vasculature[5].

To confirm the specificity of fibrin clot formation, anti-fibrin-specific mAbs were administered to mouse bearing both tumor and traumatic wound. The anti-fibrin mAbs disap-

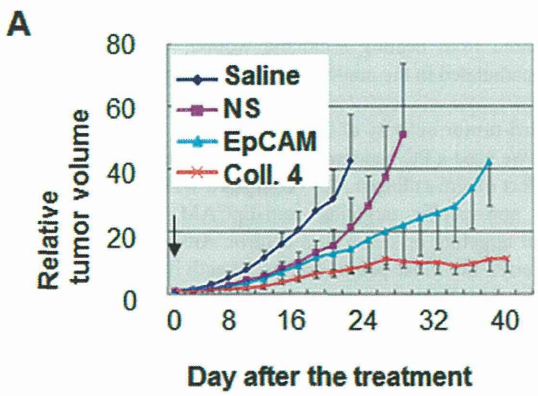

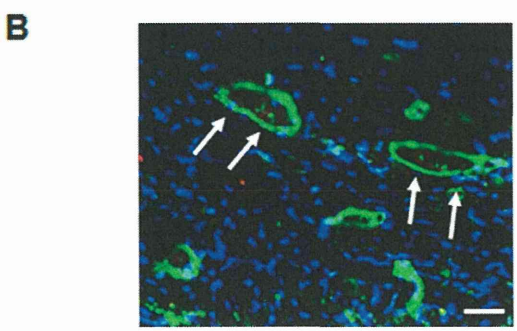

Fig. 5. Anti-collagen IV ADC. (A) Anti-tumor effect of anti-collagen IV ADC (Coll.4) was compared with control (saline), non-specific mAb ADC (NS) and anti-EpCAM ADC (EpCAM). SN-38 is used as the payload. (B) Damaged tumor vasculature immunostained by CD31 (red), collagen IV (green) and DAPI (blue) is shown. Arrow indicates CD31-negative, collagen IV-positive ring structure. Scale bar, 20 μm.